land

MDPI

Article

Improving Dryland Urban Land Cover Classification Accuracy Using a Classical Convolution Neural Network

Wenfei Luan [1], Ge Li [1,*], Bo Zhong [2], Jianwei Geng [3], Xin Li [4], Hui Li [1] and Shi He [1]

[1] School of Surveying and Land Information Engineering, Henan Polytechnic University, Jiaozuo 454000, China; luanwf@hpu.edu.cn (W.L.); 212104010008@home.hpu.edu.cn (H.L.); heshi@hpu.edu.cn (S.H.)
[2] Key Laboratory of Digital Earth Science, Aerospace Information Research Institute, Chinese Academy of Sciences, Beijing 100101, China; zhongbo@aircas.ac.cn
[3] Key Laboratory of Watershed Geographic Sciences, Nanjing Institute of Geography and Limnology, Chinese Academy of Sciences, Nanjing 210008, China; jwgeng@niglas.ac.cn
[4] National Tibetan Plateau Data Center, State Key Laboratory of Tibetan Plateau Earth System, Environment and Resources, Institute of Tibetan Plateau Research, Chinese Academy of Sciences, Beijing 100101, China; xinli@itpcas.ac.cn
* Correspondence: lige0607@hpu.edu.cn

Abstract: Reliable information of land cover dynamics in dryland cities is crucial for understanding the anthropogenic impacts on fragile environments. However, reduced classification accuracy of dryland cities often occurs in global land cover data. Although many advanced classification techniques (i.e., convolutional neural networks (CNN)) have been intensively applied to classify urban land cover because of their excellent performance, specific classification models focusing on typical dryland cities are still scarce. This is mainly attributed to the similar features between urban and non-urban areas, as well as the insufficient training samples in this specific region. To fill this gap, this study trained a CNN model to improve the urban land classification accuracy for seven dryland cities based on rigorous training sample selection. The assessment showed that our proposed model performed with higher overall accuracy (92.63%) than several emerging land cover products, including Esri 2020 Land Cover (75.55%), GlobeLand30 (73.24%), GLC_FCS30-2020 (69.68%), ESA WorldCover2020 (64.38%), and FROM-GLC 2017v1 (61.13%). In addition, the classification accuracy of the dominant land types in the CNN-classified data exceeded the selected products. This encouraging finding demonstrates that our proposed architecture is a promising solution for improving dryland urban land classification accuracy and compensating the deficiency of large-scale land cover mapping.

Keywords: dryland region; urban land classification; convolution neural network; training sample

Citation: Luan, W.; Li, G.; Zhong, B.; Geng, J.; Li, X.; Li, H.; He, S. Improving Dryland Urban Land Cover Classification Accuracy Using a Classical Convolution Neural Network. *Land* **2023**, *12*, 1616. https://doi.org/10.3390/land12081616

Academic Editors: Kathryn Sheffield, Mohammad Abuzar and Alison L. Cowood

Received: 30 June 2023
Revised: 6 August 2023
Accepted: 14 August 2023
Published: 16 August 2023

1. Introduction

Over the past decades, cities in dryland regions have experienced radical land cover changes due to rapid urbanization. Since the dryland region is more fragile and sensitive to anthropogenic activities and climate change [1], the urban land dynamics of dryland regions would lead to intensive environmental problems, such as land degradation, water scarcity, and even biodiversity loss [2–4]. To our knowledge, drylands cover nearly 41.3% of the surface and are home to 2.1 billion people [5]. The recent rapid increase in the population of dryland regions, such as Central Asia and Northwest China, has inevitably facilitated regional urban land expansion and exacerbated environmental problems to harm sustainable development [4].

Accurate land cover data are a key to support policy making in managing dryland sustainable urbanization. Traditional large-scale land cover classification techniques generally adopt auxiliary information analysis from satellite imagery to improve classification accuracy based on spectral classification models. However, most of their accuracy is limited in dryland regions because of the common misclassifications among the dominant land types, such as bare land, sparse vegetation, and built-up areas, due to a spectral confusion problem [6,7]. In addition, similar features among the above land types in dryland cities enhance the difficulty of sample selection for urban land cover classification model training, which significantly constrains the application of advanced classification models (i.e., convolutional neural networks (CNN)) in this special region [8]. Therefore, developing a specific classification workflow for a dryland city would be a potential solution to address the deficiency of large-scale land cover mapping.

Drylands are located in various climatic zones with different climatic characteristics [9], indicating that a stable and robust model is required for dryland urban land classification which is consistent with the demand for global land cover mapping. Thirty-meter spatial resolution land cover is acknowledged as the most appropriate scale to monitor urban land dynamics [10]; several emerging global fine-resolution products (10–30 m) may provide a viable option for revealing urban land changes in dryland regions, but their utility has not been well verified [11]. Taking GlobeLand30 as an example, this dataset is produced mainly based on Landsat imagery, which is recognized as one of the representative finer-resolution products with an overall accuracy of 80.33% at a global scale [12], but inconsistent accuracy across different regions still exists in this product. A previous study evaluated the accuracy of GlobeLand30 in central Asia and found that its overall accuracy was only 46% [13]. The spatial inconsistency of different land types in dryland regions among the new emerging products, such as FROM-GLC30-2020, GLC_FCS30, and GlobeLand30, reached 65.96% [14]. To this end, some researchers have pointed out the common problem that land cover mapping based on Landsat imagery using traditional spectral classification techniques is not as reliable in dryland areas as in other regions; the reason is that urban and non-urban areas of this imagery showed no distinct difference in spectral response [15–17]. Therefore, it is foreseeable that there will be reduced accuracy of dryland land cover classification in several global thematic maps which focus on urban land mapping [17–19].

In the era of 'big earth data', increasing amounts of remote sensing data are available from the observations of sensors and models [20,21]. Meanwhile, many innovative approaches have been applied to deal with these complex data [22,23], which also benefits the improvement of urban land cover classification techniques [24,25]. In that respect, CNN is a widely used technique in object recognition owing to its remarkable performance [26]. This model excels in extracting deep and hierarchical features from remote sensing data to handle land cover classification tasks [27–29]. For example, Memon et al. [30] trained a CNN model to classify land cover in Maharashtra state, India, using synthetic aperture radar (SAR) data: the overall accuracy of their proposed model reached 98.38%. With advances in high-resolution imagery acquisition, numerous studies have also obtained promising classification accuracy based on high-resolution imagery using different CNN models [31–33]. Nevertheless, the CNN model has not been thoroughly explored for urban land cover classification of dryland cities, which is probably because abundant labeled samples are indispensable for CNN model training, but few samples have been labeled for this region because it is difficult to accurately distinguish urban from non-urban areas.

Existing work focused on the application of traditional shallow machine learning algorithms combined with medium-resolution data to identify dryland land cover [34,35]. For instance, Zhu et al. [36] obtained satisfactory classification results by integrating meteorological data and vegetation indices derived from Landsat imagery to detect irrigated dryland distribution changes using a random forest classifier. Likewise, Weng et al. [37] identified typical landscapes, such as deserts, oasis, Gobi, and water systems, at an acceptable level based on the spectral information of HJ-1A/1 B imagery and an improved gcForest algorithm. However, the above classified data focusing on dryland-dominant land types provide limited support for complex urban land cover classification. Several other studies also demonstrated the feasibility of classic machine learning techniques to reveal detailed dryland surface compositions (i.e., water, urban area, cropland, forest, and bare soil) using Landsat or Sentinel images [38,39]. Recently, Ali et al. [34] adopted the spectral band combination training strategy of Sentinel imagery to handle dryland urban cover classification with a CNN model; barren land, settlements, fallow land, vegetation, and water bodies were discriminated with high accuracy. Since this work was conducted in several small, urbanized areas of Pakistan, the suitability of their proposed band combination model might vary in other regions. To date, high-resolution imagery has rarely been applied in the abovementioned studies. Given the rich landscape features captured by high-resolution satellite imagery, training a CNN model using high-resolution samples to classify urban land cover could be a promising approach to enhance classification accuracy for dryland cities.

Overall, this study attempts to provide a complementary solution for improving large-scale land cover mapping accuracy in a dryland region at a resolution of 30 m using a classical CNN model. To achieve this goal, we first selected seven typical dryland cities located in central Asia and northwest China as our research area. Second, the urban land cover of each city was classified based on high-resolution Google Earth imagery and a trained CNN model; it should be noted that the classification model was trained using specific samples for dryland regions. Finally, we evaluated the accuracy of our results using visual validation. The classification results were also compared with several global finer-resolution land cover products to verify the advantages of the CNN classification architecture.

2. Materials and Methods

2.1. Study Area

The dryland region is defined by precipitation, which refers to the area where the mean annual precipitation is less than 500 mm [40,41]. This study selected seven cities located in typical dryland regions, including Lanzhou, Xining, Urumqi, Kabul, Tashkent, Bishkek, and semi-arid Lahore, as the study area (Figure 1 and Table 1). Lahore was selected because approximately 75% of the annual total rainfall occurs from June to September [42], indicating this city exhibits arid characteristics throughout most of the year. The total area of the study region is 5635 square kilometers. Various land types, such as bare land, sparse vegetation, cultivated land, impervious surfaces, and ice and snow in urban and suburban regions, compose most areas of the landscapes in the selected cities. Considering the common misclassifications among the major land types, such as sparse vegetation, built-up areas, and bare land, due to the spectral confusion problem in this region, the region is an ideal experimental area to enhance dryland urban land classification accuracy.

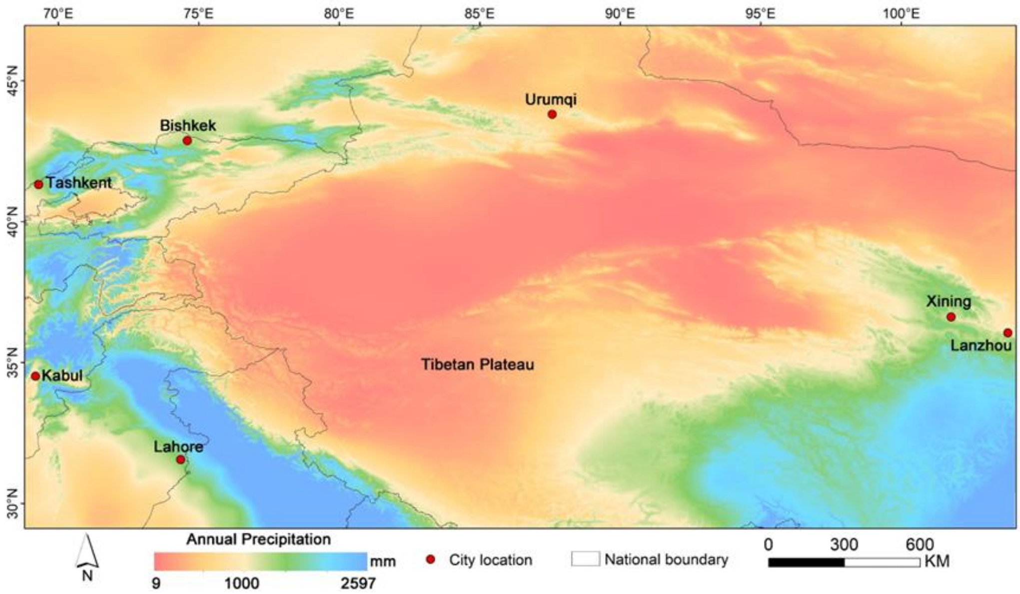

Figure 1. Location of the study cities in the dryland region (precipitation data are available at http://worldclim.org (accessed on 21 April 2021)).

Table 1. Introduction of the studied cities in a typical dryland region.

City	Climate	Annual Mean Precipitation (mm)	Annual Mean Temperature (°C)
Urumqi, China	Continental cold semi-arid climate	286	7.8
Xining, China	Cold semi-arid climate	374	6.1
Lanzhou, China	Semi-arid climate	312	10.9
Lahore, Pakistan	Semi-arid climate	628	24.0
* Kabul, Afghanistan	Cold semi-arid climate	312	12.1
* Tashkent, Uzbekistan	Mediterranean climate	444	14.1
* Bishkek, Kyrgyzstan	Mediterranean-influenced humid continental climate	453	9.8

Notes: Cities marked with * are national capitals, the rest are provincial capitals.

2.2. Materials and Classification Workflow

This study selected high-resolution imagery as raw data to conduct urban land classification based on a CNN model trained on typical dryland landscape samples. The classification accuracy was also compared with that of several global finer-resolution land cover products. The detailed workflow of the research process is shown in Figure 2.

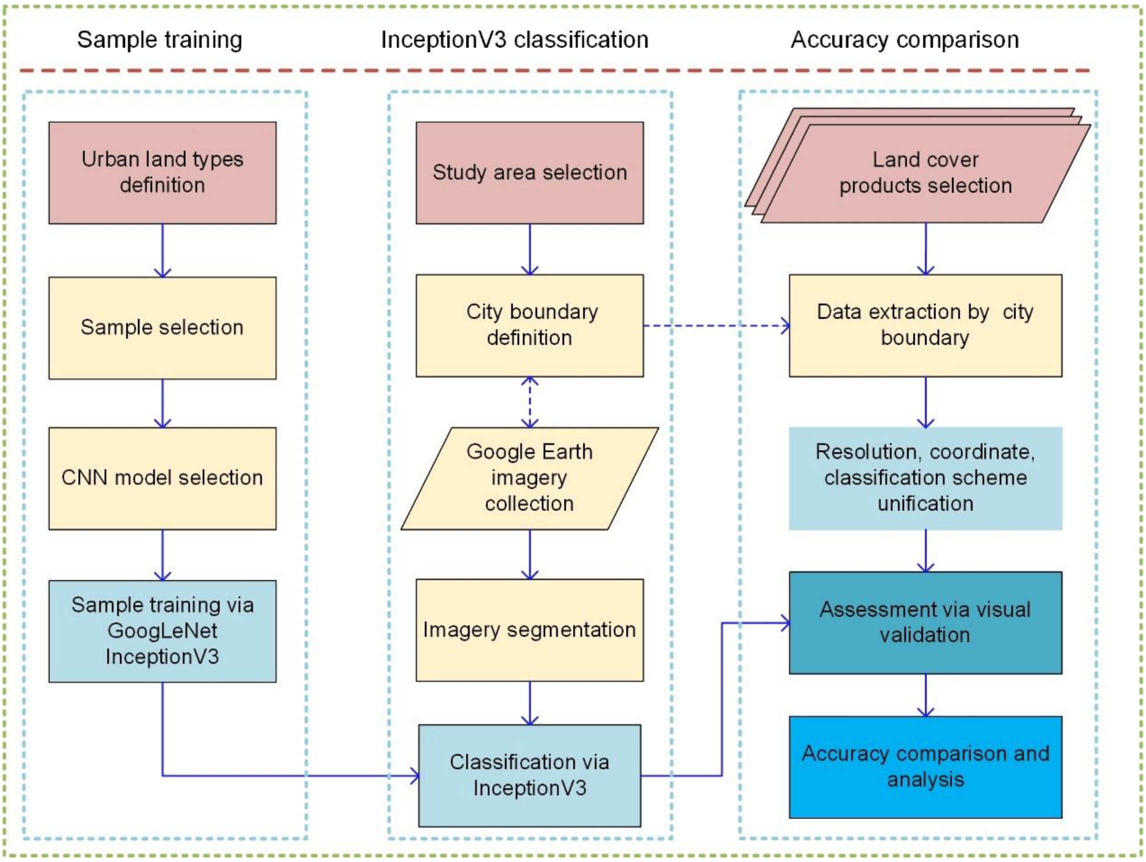

Figure 2. Workflow for improving urban land classification accuracy in dryland regions.

2.2.1. Data for Classification

Historical (2017) Google Earth high-resolution (0.6 m) imagery was selected as raw data for urban land classification. This satellite imagery is composed of three spectral bands, including red, green, and blue, which is well suited for image categorization using the CNN architecture. The year 2017 was selected because abundant land cover products around this year can support the improvement verification of our method through map comparison. The city boundary was defined using the intersection area between the Database of Global

Administrative Areas (https://gadm.org/data.html (accessed on 16 July 2022)) and the available Google Earth imagery area of each city.

2.2.2. CNN Model Selection

To date, numerous CNN models have been designed to tackle land cover classification problems; recent studies have proven that the GoogLeNet inceptionV3 model is effective and efficient for land cover type identification based on high-resolution imagery [43–45]. Compared with typical CNN models, inceptionV3 introduced the new concept of separable convolutional layers, which can reduce the number of computing parameters and significantly improve the feature learning speed [46–48]. However, training the land cover sample of this architecture from scratch requires large amounts of labeled data to generate high accuracy classification results. This strategy inevitably costs a great deal of computational resources, considering the millions of parameters that need to be learned. Previous studies have demonstrated that a fine-tuned InceptionV3 outperformed the original model in some specific classification tasks because it can extract additional features from the target samples with a reduced computational cost [49,50]. To enhance computing efficiency, a fine-tuned GoogLeNet inceptionV3 model was employed in this study to yield reliable urban land cover data for dryland cities.

2.2.3. Model Training and Urban Land Cover Classification

To our knowledge, most urban land cover classification research has adopted a simple classification scheme to detect urban land dynamics; this is attributed to the land composition in urban areas not being as complicated as that at a regional or global scale [51]. To make the classification results comparable, this study set the classification system as vegetation, cultivated land, artificial surfaces, water bodies, and others (Figure 3) based on a universal UN LCCS (United Nations Land Cover Classification System) aggregation [52].

Figure 3. Examples of the training samples derived from Google Earth high-resolution imagery.

The aim of model training was to extract distinct features of each land type from specific samples in a typical dryland region using a pre-trained InceptionV3 model. To achieve this goal, typical dryland samples were extracted from a public benchmark dataset derived from Google Earth high-resolution imagery for model training. This dataset covered abundant labeled land types in China (i.e., cultivated land, forest, grassland, shrubland, water bodies, artificial surfaces, bare land, and permanent snow and ice) [43]. First, 10,000 labeled images of each land type in typical dryland regions were randomly selected as training samples based on their geographical location (Figure 3). Then, the above sample was aggregated in line with our defined classification scheme; this process followed GlobeLand30 aggregation (Section 2.3.2).

During the model training process, the global features of imagery that contained multiscale and nonlinear characteristics were reserved in the pre-trained InceptionV3 model, and only the first layer of InceptionV3 was fine-tuned based on the selected sample. In that respect, 85% of the selected samples were used for model training and the rest were prepared for model verification. The initial learning rate was set as 0.01 at the beginning of the training process and then updated to 0.0001 after 90% of the iteration period was completed. The training process was completed when the training accuracy approximated the verification accuracy. In addition, the training accuracy and verification accuracy were calculated using the output of the softmax classifier.

Since the trained model could assign the entire image to a specific land type, the raw imagery of each city was segmented into a large number of images arranged by their geographical coordinates. To capture more texture information from the surrounding pixels, the size of the segmented images was set as 3×3 pixels centered on the unclassified pixel. Serving as the inputs of the InceptionV3 classification model, the segmented images were identified using the powerful parallel computing mechanism embedded in the TensorFlow platform. Once the probabilities of land type were obtained from the Softmax classifier based on the fine-tuned InceptionV3 model, the maximum probability land type was selected to categorize the unclassified pixels. After all images were identified, the final land cover map was created using the pixel location information and its classified label.

It also should be noted that the model training and classification process were conducted using TensorFlow (version 2.4.1) on the Windows 10 operation system. To improve the model training efficiency, an Nvidia GeForce RTX 3090 24G GPU was configured on the computing platform.

2.3. Assessment of Urban Land Classification

2.3.1. Visual Validation

Visual validation through confusion matrix analysis was used to assess classification accuracy. Interpreting reference data from high-resolution imagery is a common strategy for land cover classification accuracy assessment [53,54]. To obtain all land types for the accuracy assessment, dense validation points were collected in the study cities as reference data. These points were randomly selected and visually interpreted from high-resolution Google Earth images. The nearest distance between each point was set as 500 m. The total number of reference points remained at 2022 after some poor-quality points were eliminated (Figure 4). Additionally, the kappa coefficient, overall accuracy (OA), user accuracy (UA), and producer accuracy (PA), combined with commission errors (CE) and omission errors (OE) derived from the confusion matrix, were used to evaluate the classification accuracy.

2.3.2. Comparison with Five Existing Land Cover Products

To demonstrate the improvement of CNN in dryland urban land cover classification, five burgeoning global finer-resolution land cover products, namely GlobeLand30 (30 m) 2020 provided by the National Geomatics Center of China (NGCC) [55], FROM-GLC 2017v1 (30 m) developed by Gong et al. [56], GLC_FCS30-2020 generated by Zhang [57], Esri 2020 Land Cover (10 m) released by Karra et al. [58], and ESA WorldCover2020 (10 m) produced by the European Space Agency [59], were adopted to evaluate the improvement of CNN classification through map accuracy comparison. Despite the epochs of the selected products focused on 2017 or 2020, the land cover was seemingly unlikely to experience a significant change during such a short period. Comparison datasets, such as GlobeLand30, FROM-GLC 2017v1, and GLC_FCS30-2020, were produced by screening high-quality Landsat imagery around its target epoch, which indicated that our selected products were suitable for accuracy comparison even if their epochs were inconsistent. Furthermore, we re-projected all the selected data (except GlobeLand30) to the UTM projection as GlobeLand30. The resolution of these datasets was resampled to 30 m using the nearest sampling technique. Land types of different classification schemes were aggregated into vegetation, cultivated land, artificial surfaces, water bodies, and others (Table 2), following the work of Tsendbazar et al. [60].

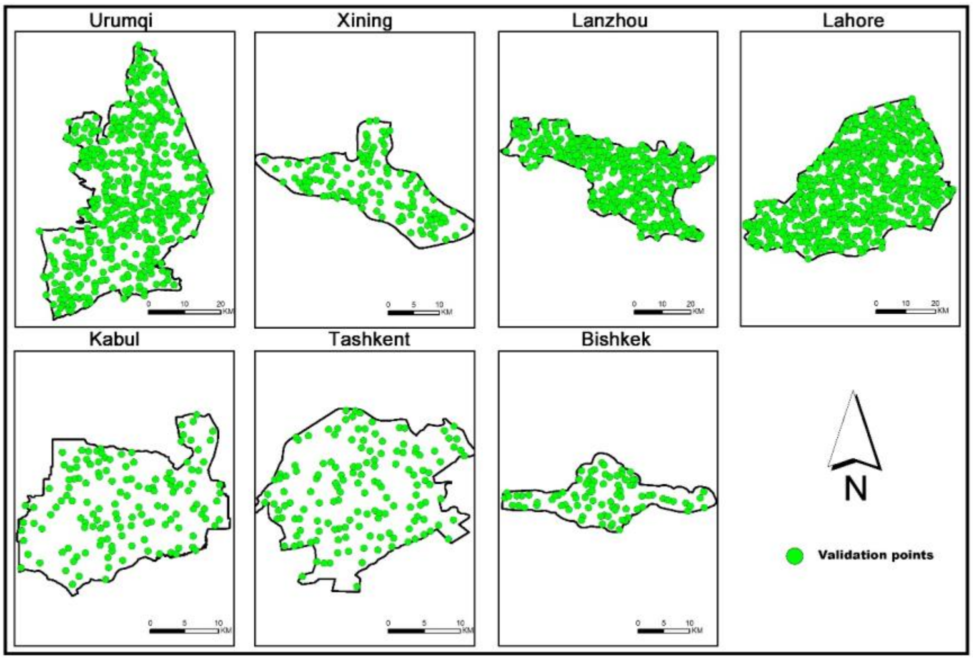

Figure 4. Distribution of validation points for each city.

Table 2. Aggregated land cover classes and their definitions (Notes: The numbers of each product represent the original classification scheme codes. V: Vegetation; C: Cultivated land; A: Artificial surfaces; W: Water bodies; O: Others).

Land Cover Types	GlobeLand30-2020	FROM-GLC 2017v1	GLC_FCS30-2020	Esri 2020 Land Cover	ESA World-Cover2020	Definition
V	20, 30, 40, 50	2, 3, 4, 5	50, 60, 61, 62, 70, 71, 72, 80, 81, 82, 90, 120, 121, 122, 130, 180	2, 4, 11	10, 20, 30, 90	Lands where forests, shrubs, and natural grass cover is at least 10% of the total area and lands.
C	10	1	10, 11, 12, 20	5	40	Lands where crops occupy more than 40% of the total area.
A	80	8	190	7	50	Lands covered by man-made structures, such as buildings and roads.
W	60	6	210	1	80	Water bodies locate in the land area.
O	70, 90, 100	9,10	150, 152, 153, 200, 201, 202, 220	8, 9, 10	60, 70	Lands covered by permanent snow, glaciers, and icecaps, or lands with vegetation cover less than 10%.

3. Results

3.1. Assessment of GoogLeNet InceptionV3 Classification Results

The visual validation results for each land cover dataset are listed in Table 3. Herein, the Kappa coefficient can be used to evaluate the overall agreement of the classification [61]. According to the Kappa coefficient interpretation of Landis and Koch [62] (Table 4), only the InceptionV3-classified data reached an almost perfect level; Esri 2020 Land Cover and GlobeLand30 also performed well at a substantial agreement level, while the rest of the datasets showed moderate agreement because their Kappa coefficient ranged from 0.46 to 0.56. Similarly, the OA of the InceptionV3-classified data (92.63%) also outperformed the compared products, suggesting the high reliability of our proposed model.

Table 3. Accuracy assessment of several land cover products. Bold font numbers represent the OA of corresponding products (V: Vegetation; C: Cultivated land; A: Artificial surfaces; W: Water bodies; O: Others).

	Products	Type	Reference Data					UA (%)	Kappa Coefficient
			V	C	A	W	O		
Classified data	InceptionV3 classified data	V	358	7	8	3	6	93.72%	0.89
		C	45	550	22	3	16	86.48%	
		A	4	4	850	0	2	98.84%	
		W	2	1	0	8	3	57.14%	
		O	20	0	3	0	107	82.31%	
		PA (%)	83.45%	97.86%	96.26%	57.14%	79.85%	**92.63%**	
	GlobeLand30	V	195	108	65	2	12	51.05%	0.60
		C	47	549	35	1	4	86.32%	
		A	30	103	722	3	2	83.95%	
		W	1	3	0	10	0	71.43%	
		O	81	29	13	2	5	3.85%	
		PA (%)	55.08%	69.32%	86.47%	55.56%	21.74%	**73.24%**	
	FROM-GLC 2017v1	V	219	62	39	0	62	57.33%	0.46
		C	104	495	21	1	15	77.83%	
		A	178	105	477	1	99	55.47%	
		W	4	1	1	5	3	35.71%	
		O	54	19	16	1	40	30.77%	
		PA (%)	39.18%	72.58%	86.10%	62.50%	18.26%	**61.13%**	
	GLC_FCS30-2020	V	178	118	49	0	37	46.60%	0.56
		C	65	492	49	3	27	77.36%	
		A	76	62	700	1	21	81.40%	
		W	2	4	0	7	1	50.00%	
		O	66	25	6	1	32	24.62%	
		PA (%)	45.99%	70.19%	87.06%	58.33%	27.12%	**69.68%**	
	Esri 2020 Land Cover	V	235	73	61	2	11	61.52%	0.63
		C	127	463	43	1	2	72.80%	
		A	25	21	802	5	7	93.26%	
		W	0	1	0	11	2	78.57%	
		O	95	0	14	1	6	5.17%	
		PA (%)	48.76%	82.97%	87.17%	55.00%	21.43%	**75.55%**	
	ESA World-Cover2020	V	193	45	24	1	119	50.52%	0.52
		C	92	442	16	2	84	69.50%	
		A	65	34	580	2	179	67.44%	
		W	0	1	0	9	4	64.29%	
		O	60	12	7	2	130	61.61%	
		PA (%)	47.07%	82.77%	92.50%	56.25%	25.19%	**64.38%**	

Table 4. Interpretation of the Kappa coefficient [62].

Kappa	0.8–1.0	0.6–0.8	0.4–0.6	0.2–0.4	0.0–0.2	Negative
Performance	Almost perfect	Substantial	Moderate	Fair	Slight	Poor

Regarding the performance of individual land types, it should be noted that artificial surfaces were well identified based on the high PA (96.26%) and UA (98.84%). In addition, the InceptionV3-classified data also showed desirable accuracy for vegetation, cultivated land, and others because nearly all their PA and UA exceeded 80%. In this respect, the PA of vegetation and cultivated land were 83.45% and 97.86%, respectively. Meanwhile, their UA values were 93.72% and 86.48%, respectively. Nevertheless, minor misclassifications were still observed between vegetation and cultivated land. Given that shrubs and natural grass cover, which are part of the vegetation, likely coexist sparsely with crops in pixels dominated by cultivated land, minor errors are inevitable among these mixed pixels. Similar features in vegetation and crops during the growing season also enhance the difficulty of distinguishing vegetation regions from cultivated land. In the case of others, its PA and UA were 79.85% and 82.31%, respectively, which were slightly lower than those of vegetation and cultivated land. As Google Earth high-resolution imagery is a composite of yearly data merged from high-quality images captured on different dates throughout the year, land types at the same location may vary across different seasons. This phenomenon can be particularly discovered in the other land types, such as vegetation and cultivated land. For instance, crops or vegetation-covered regions may be classified as others during the nongrowing season, which complicates the identification of others. Water bodies showed the lowest PA and UA (both were 57.14%) of the five classes; however, this land type occupied the smallest fraction of the study area. Low PA and UA levels in water bodies cannot significantly influence OA.

3.2. Accuracy Comparison Results

3.2.1. Accuracy Comparison with Five Existing Land Cover Products

The accuracy of several global emerging land cover products was compared with InceptionV3 classified data. According to Table 3, the OA of the selected land cover products ranked in descending order were the following: Esri 2020 Land Cover (75.55%), GlobeLand30 (73.24%), GLC_FCS30-2020 (69.68%), ESA WorldCover2020 (64.38%), and FROM-GLC 2017v1 (61.13%). All their OA were much lower than the InceptionV3-classified data (92.63%). CE and OE are also shown in Figure 5 to describe the misclassifications of individual land types for the comparison datasets. Almost all the CE and OE in InceptionV3-classified data were significantly lower than in the other data.

Artificial surfaces in GlobeLand30, GLC_FCS30-2020, and Esri 2020 Land Cover were better identified than the other land types (Figure 5) because both their PA and UA exceeded 81% (Table 3). This finding was consistent with the InceptionV3 classification data. However, the accuracy of artificial surface identification was still far behind that of our data (Figure 5). As for FROM-GLC 2017v1 and ESA WorldCover2020, artificial surfaces were poorly discriminated with a higher CE and OE, which probably constrained their application in dryland urbanization research. With regard to vegetation, nearly all selected products failed to capture its distribution accurately. Most of their PA and UA were around 50%, indicating that roughly half of the vegetation in the selected products was likely to be misclassified (Figure 5). In contrast, cultivated land was identified more accurately because most of their PA and UA surpassed 70%. Nevertheless, none of them performed better than InceptionV3-classified data (Figure 5). The PA and UA of water bodies in different datasets ranged from 35.71% to 78.57%; more than half were below 60%, suggesting that water body discrimination was not satisfactory, which agreed with the InceptionV3-classified data. Nevertheless, unexpected CE and OE of the smallest fraction of land type would have a limited impact on the OA of these selected datasets. The identification of others encountered the most significant challenge because all the products presented the poorest

CE and OE for this land type. In contrast, only our data achieved an encouraging level of classification accuracy for others with acceptable PA (82.31%) and UA (79.85%).

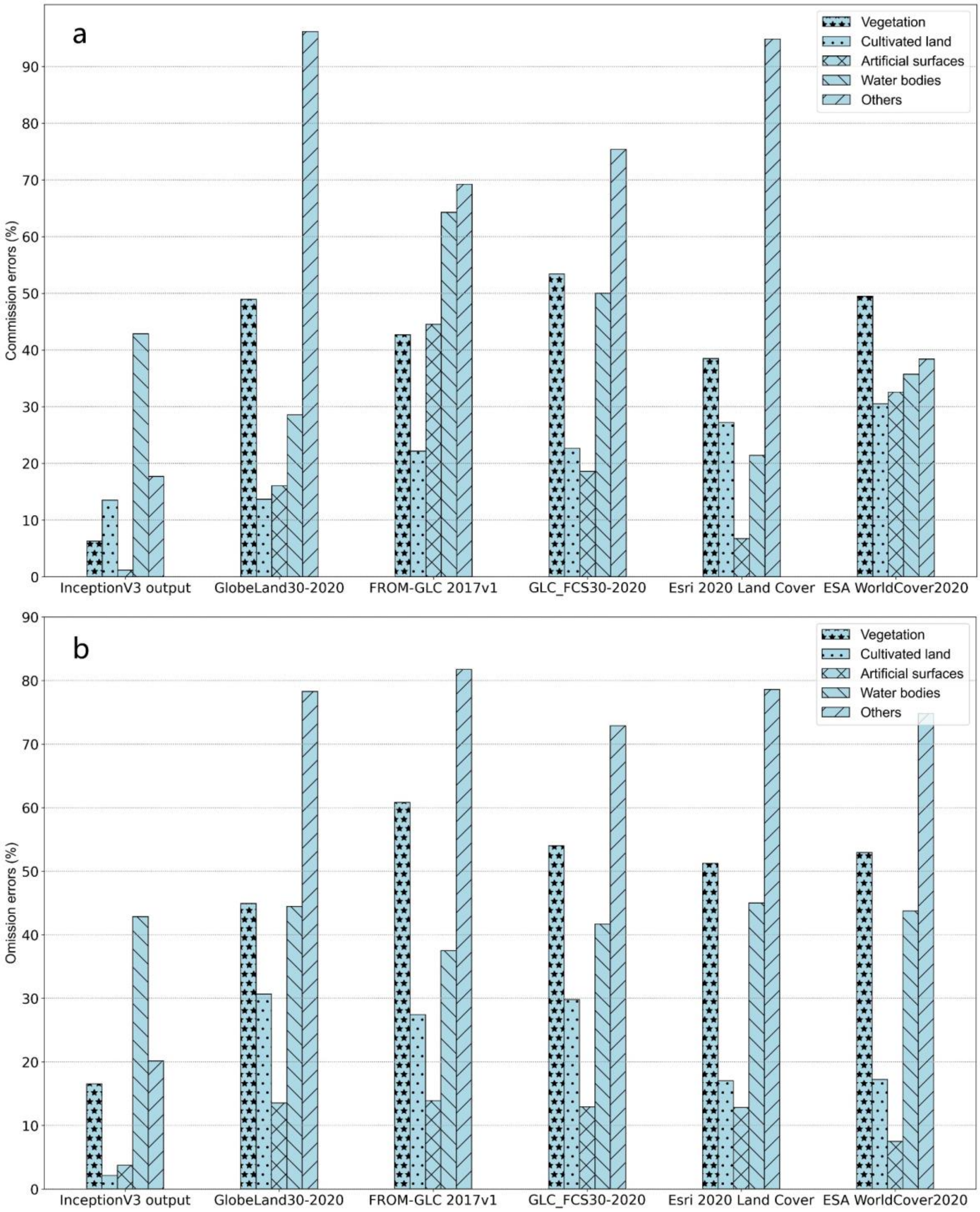

Figure 5. Commission errors and omission errors of each land cover data. (**a**) commission errors. (**b**) omission errors.

3.2.2. Misclassification of Each Dataset

Figure 6 quantitatively illustrated the misclassification of each comparison dataset. Taking InceptionV3 output as an example, the arrow direction from V to C denoted that part of the vegetation was misclassified as cultivated land. The width of the lines represented the number of misclassified points, with wider lines indicating more misclassified points. The remaining lines were plotted following the same principle. The number of misclassified points was derived from the visual validation results. Figure 6 demonstrated that the InceptionV3-classified data outperformed the other dataset because of its slight misclassification. To describe the comparison concisely, only the most significant misclassification of each dataset was analyzed. For GlobeLand30 and GLC_FCS30-2020, cultivated land was significantly misclassified as vegetation. Similar misclassification was also found in the Esri 2020 Land Cover. Plenty of artificial surfaces were identified as vegetation, cultivated land, and others in FROM-GLC 2017v1. Others were poorly classified into vegetation, cultivated land, and artificial surfaces in ESA World-Cover2020. Dominant misclassification in InceptionV3 output occurred between vegetation and cultivated land. Nonetheless, this confused error remained considerably lower than that in the other dataset.

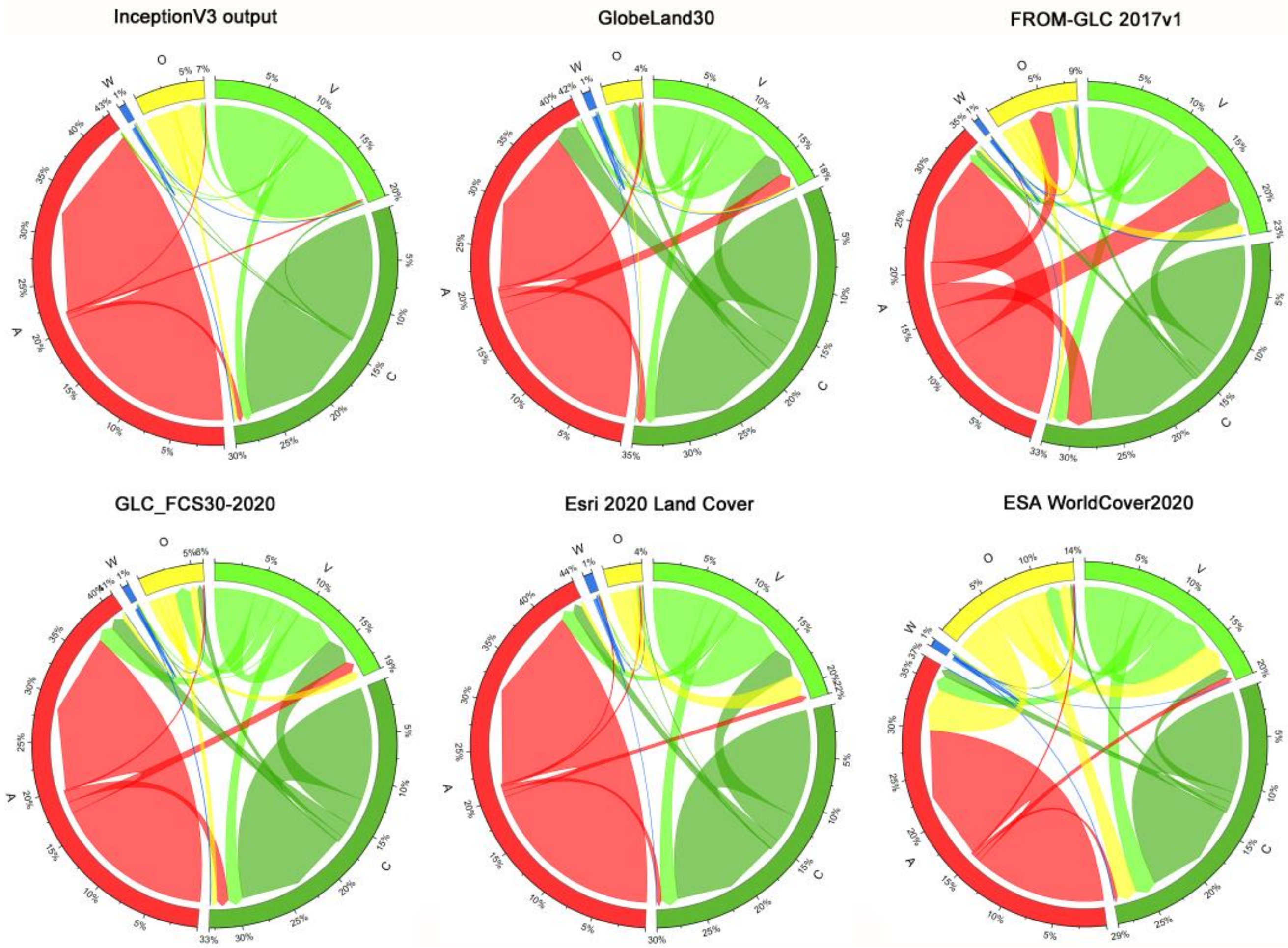

Figure 6. Confused classification errors of the comparison datasets. (V: Vegetation; C: Cultivated land; A: Artificial surface; W: Water body; O: Others).

3.2.3. Statistical and Spatial Variation among Different Datasets

Both statistical and spatial distribution inconsistencies of different land types were found among the comparison products and the InceptionV3-classified data (Figures 7 and 8). Statistical results showed that the vegetation appeared to be similar across the InceptionV3-classified data, GLC_FCS30-2020, Esri 2020 Land Cover, and ESA WorldCover2020. Given that the InceptionV3 output provided the best classification result based on its high accuracy, vegetation occupation was underestimated in GlobeLand30 but overestimated in FROM-GLC 2017v1. The cultivated land area was around 1500 km^2 in InceptionV3 output, Esri 2020 Land Cover, and ESA WorldCov-er2020, but it was commonly overestimated in the of the rest products, especially in GlobeLand30. Similar areas of artificial surfaces were observed in four datasets: InceptionV3 output, GlobeLand30, GLC_FCS30-2020, and Esri 2020 Land Cover, but this land type was significantly underestimated in FROM-GLC 2017v1 and ESA WorldCover2020. Water bodies were the unique land types that showed consistent areas for all the comparison datasets. The most significant unconformity occurred in others. It should be noted that severe underestimation of others was found in GlobeLand30 and Esri 2020 Land Cover. In contrast, this land type was distinctly overestimated in ESA WorldCover2020.

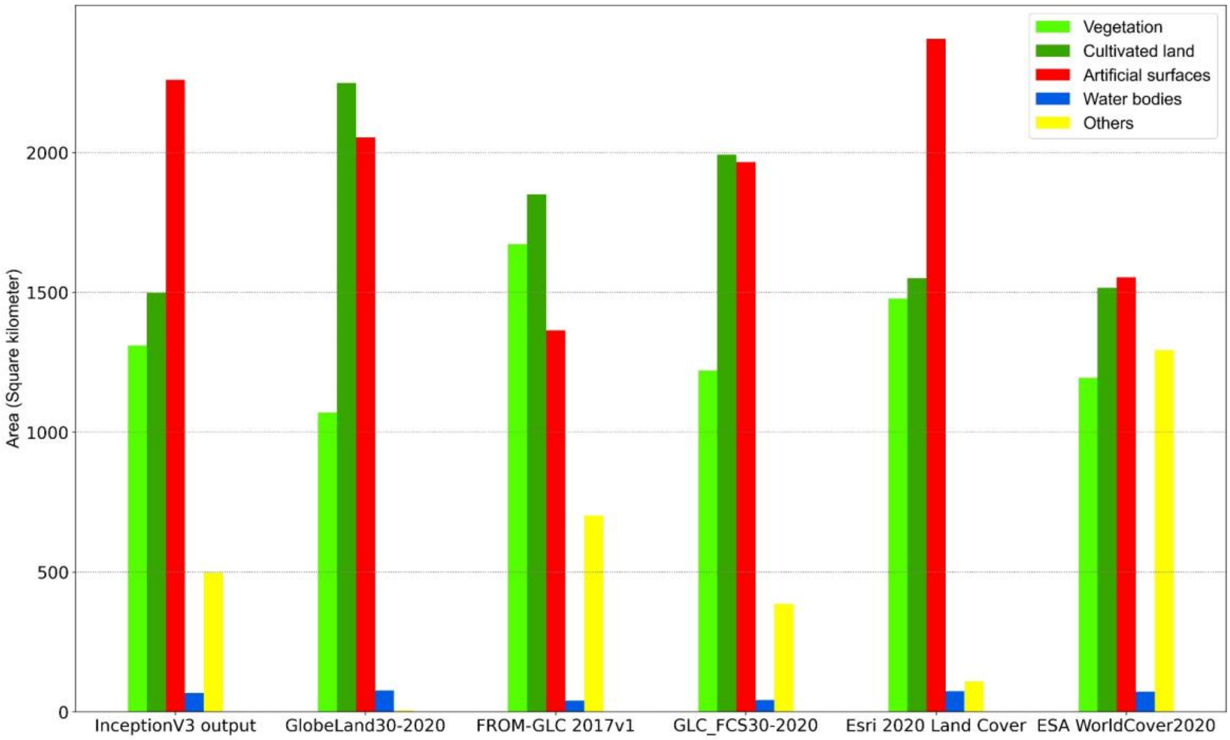

Figure 7. Statistical area of different land types for the comparison products and InceptionV3-classified data.

Spatial distribution variations were found in all selected cities. Taking Urumqi city (Figure 8) as a sample, it can be observed that most of the comparison datasets exhibited a similar distribution of water bodies. However, vegetation, cultivated land, and others confusion were a general problem for almost all the selected datasets. Specifically, a substantial amount of vegetation was misclassified as others in FROM-GLC 2017v1, GLC_FCS30-2020, and ESA WorldCover2020. Confusion between vegetation and cultivated land was evident in southeast Urumqi for GlobeLand30. InceptionV3-classified data can discriminate vegetation, cultivated land, and others effectively. The spatial distribution of artificial surfaces was similar in all the comparison datasets except FROM-GLC 2017v1, which was attributed to its poor 10.5% producer accuracy and 30.8% user accuracy provided by its producer. Sparsely distributed artificial surfaces were often neglected for most products, especially for GLC_FCS30-2020 and Esri 2020 Land Cover.

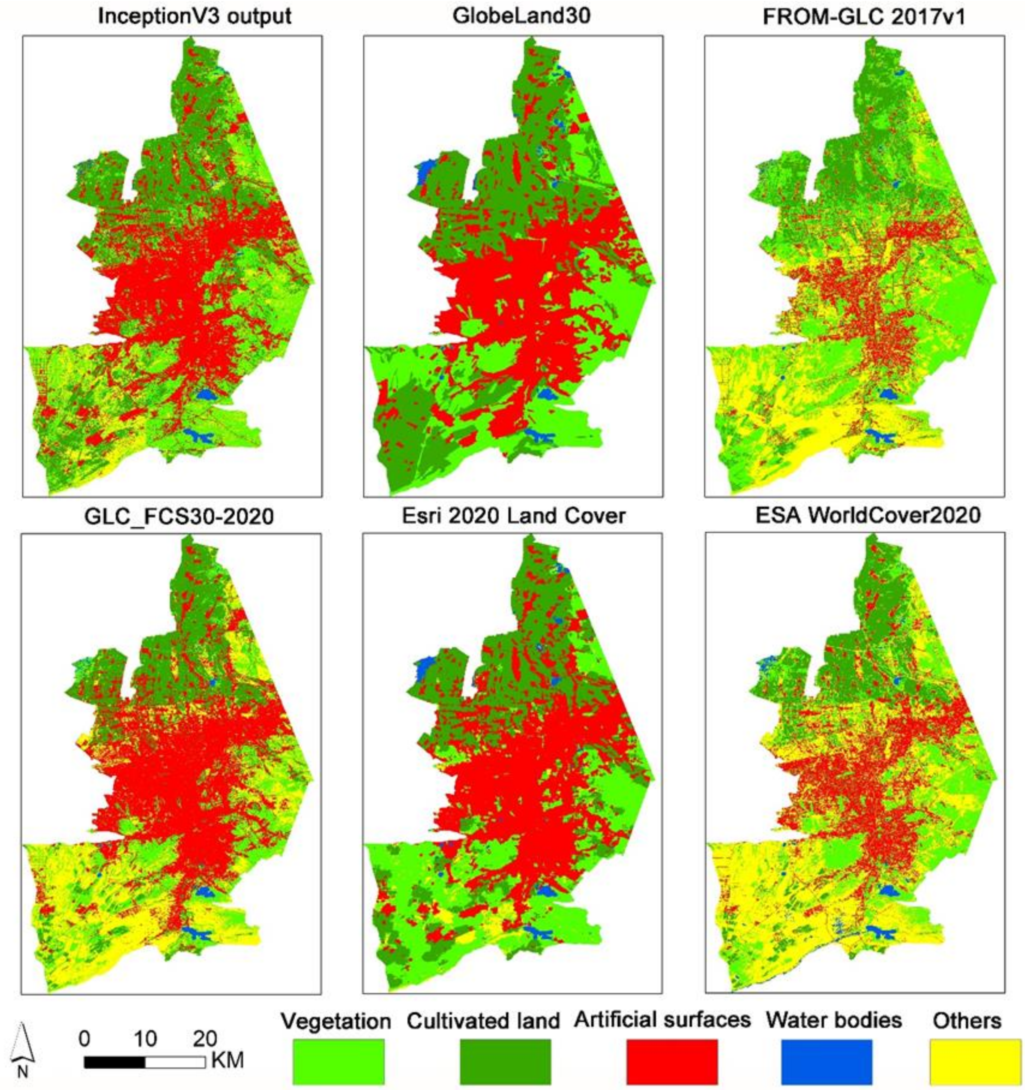

Figure 8. Urban land cover comparison of Urumqi.

3.3. Accuracy Improved Cases of InceptionV3 Classification Model

The purpose of this section is to provide evidence supporting the advantages of the trained InceptionV3 model. A detailed map comparison was illustrated in Figure 9.

Figure 9a showed that the sparse built-up areas were easily misclassified as their surrounding land types for most of the selected products, especially in GlobeLand30, FROM-GLC 2017v1, and GLC_FCS30-2020, which probably led to the underestimation of artificial surfaces. In contrast, the InceptionV3 model was effective in accurately separating sparse artificial surfaces from surrounding land.

Figure 9b indicated that the small fraction of vegetation or cultivated land among the urbanized regions was difficult to accurately identify for most of the existing products. GlobeLand30 and Esri 2020 Land Cover screened only a portion of non-urbanized regions from high-density artificial surfaces. In addition, vegetation was misclassified as cultivated land in GlobeLand30. It was also worth noting that the vegetation regions in FROM-GLC 2017v1 and ESA WorldCover2020 were overestimated because the artificial surfaces surrounded by trees were incorrectly classified as vegetation. InceptionV3-classified data and GLC_FCS30-2020 performed better in discriminating small fractions of vegetation or cultivated land from artificial surfaces, which can provide more accurate and detailed intro-urban land information.

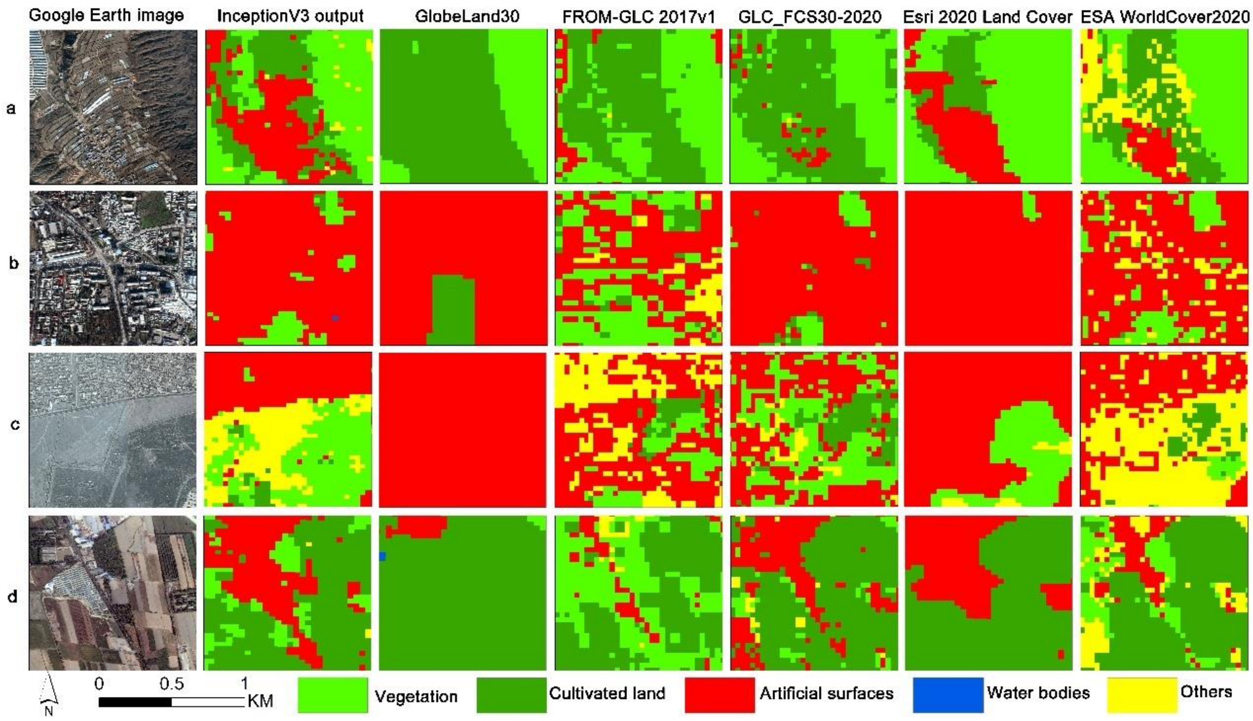

Figure 9. Classification results comparison in land cover map ((**a**): Lanzhou; (**b**): Bishkek; (**c**): Kabul; (**d**): Urumqi).

Figure 9c shows that confusion between built-up areas and bare land in arid regions was frequently observed in GlobeLand30 and Esri 2020 Land Cover. In this case, numerous pixels of bare land and artificial surfaces were inversely misclassified in FROM-GLC 2017v1. For GLC_FCS30-2020, plenty of bare land locations were identified as vegetation owing to the fact that raw imagery might be captured during the growing seasons. A similar reason also caused the overestimation of bare land for ESA WorldCover2020. Meanwhile, the InceptionV3 model depicted a more accurate land cover map because it was more consistent with the actual distribution of land types.

Figure 9d demonstrates that cultivated land and vegetation were often confused for most of the comparison products. A common reason could be that similar spectral reflectance features existing in growing crops and vegetation probably made them indistinguishable. This problem was significant in GlobeLand30, FROM-GLC 2017v1, GLC_FCS30-2020, and Esri 2020 Land Cover. Improved classification results can be found in InceptionV3-classified data and ESA WorldCover2020.

Overall, the data classified using the InceptionV3 model can provide better accuracy for the five aggregated land types than almost all the comparison products in dryland cities, indicating that the proposed model is a promising solution for dryland urban land cover classification.

4. Discussion

4.1. Reliability Analysis of Accuracy Comparison

To our knowledge, multiple classification schemes adopted by land cover producers probably led to different classification accuracies. This section discussed the influence of classification scheme aggregation on accuracy comparison. To ensure the comparability of diverse datasets under different classification schemes, this study strictly conducted classification scheme harmonization following one proven research study [60] to minimize that inconsistency effect.

Taking artificial surfaces as an example, this land type was directly converted from the products without any aggregations; subtle differences still occurred at an acceptable level because its original definition varied in different products. In that respect, urban green areas, such as parks and sport facilities, were excluded from built-up areas in the ESA WorldCover2020. Similarly, impervious surfaces in GLC_FCS30-2020, impervious in FROM-GLC 2017v1, and artificial surfaces in InceptionV3 output also adopted this classification scheme. However, interior urban green zones were classified into artificial surfaces and built areas in the GlobeLand30 and Esri 2020 Land Cover, respectively. Nevertheless, other man-made structures, including transportation facilities, buildings, and impervious roof tops, were defined as artificial surfaces for all the selected datasets. Since these man-made structures occupied the dominant artificial surfaces of urbanized areas, a slight inconsistency in the definition of artificial surfaces was acceptable for land cover classification accuracy comparisons.

Water bodies was another land type that can be directly converted from the selected products. Although its definition varied in the different datasets, no obvious differences were found in the basic content of the water bodies. Specifically, natural and artificial water-covered regions, such as lakes, rivers, reservoirs, and fish ponds, were discriminated into water bodies for the comparison datasets, suggesting a consistency of water body conversion.

The other three land types (vegetation, cultivated land, and others) were aggregated from multiple subclasses in each individual classification scheme. Although these schemes differed in certain details, they contained high consistency as well because all the schemes were designed directly or indirectly based on the universal UN LCCS, which implied that the aggregated results were comparable under the unified scheme.

Overall, slight inconsistency probably generates very limited misclassification errors that impact the classification accuracy comparison, implying that the outperformance of InceptionV3 output was reliable.

4.2. Comparative Analysis of Classification Techniques

4.2.1. Classification Technique Comparison with the Selected Land Cover Products

In this study, most of the selected products were generated using or combining spectral classification techniques, which was unlikely to provide satisfactory classification accuracy for the studied region. For instance, a classic machine learning technique, namely random forest (RF), was adopted by FROM-GLC 2017v1, GLC_FCS30-2020, and ESA WorldCover2020 to extract spectral and textural features for land cover classification. Auxiliary data, such as the normalized difference vegetation index (NDVI) and digital elevation model (DEM), were also generally applied to aid the classification process. Even then, their overall classification accuracy (less than 70%) was still lower than that of GlobeLand30, Esri 2020 Land Cover, and InceptionV3 output, indicating that the simple shallow machine learning strategy was deficient in dryland urban land cover identification.

In contrast, GlobeLand30 developed a pixel–object–knowledge (POK)-based method for land cover mapping using multispectral Landsat imagery. This method employed supervised spectral classification techniques, such as the support vector machine (SVM) and maximum likelihood classification (MLC), to classify land cover; object-based and expert knowledge-based verification were also applied to reduce misclassification errors caused by spectral confusion [12]. To some extent, this integrated method can improve the overall classification accuracy (73.24%) of the studied region, but this classification procedure was time-consuming and labor-intensive.

Since the similarity of spectral reflectance characteristics was widespread among the dominant land types of dryland regions, identifying land cover by adding spatial and texture recognition might be a promising solution to improve classification accuracy. To capture as many features of each land type as possible, the Esri 2020 Land Cover was produced via a deep learning segmentation model that had been trained using more than five billion human-labeled samples [59]. Consequently, an improved overall classification accuracy (75.55%) was achieved for the studied cities. This classification model was trained using global samples derived from various climatic zones; thus, reduced classification accuracy in drylands was foreseeable. This classification strategy requires more computational resources than the conventional classification techniques.

Taking advantage of the rich features of pre-trained InceptionV3 and incorporating deep spatial, spectral, and texture information from typical landscape samples of dryland regions, the proposed classification model can accurately identify urban land types at the expense of limited computational resources. Compared to spectral classification techniques, the spectral confusion problem can be effectively alleviated using our trained CNN model. Compared with the deep learning segmentation model, the classification accuracy of dryland urban land cover was improved using a model trained by specific samples. This finding also implied that our proposed classification workflow can serve as a supplement to improve global urban land cover accuracy for dryland cities.

4.2.2. Advantages of the Proposed Classification Workflow

Accuracy assessment demonstrated that the InceptionV3 Classification model outperformed several global land cover mapping techniques in dryland cities, which was mainly attributed to a rigorous training sample selection and rich landscape information extraction from dryland region.

Performance of DL classification is determined by the quantity and the quality of the training sample [35]. This study selected 10,000 samples of each land type from a typical dryland region for model training. Though the model generalization might be limited in large-scale land cover mapping, sufficient samples with rich dryland information can strongly represent the specific characteristics of dryland landscapes. Compared with Esri 2020 Land Cover produced using a deep learning segmentation model trained on billions of labeled samples, our fine-tuned classification model performed better in separating built-up areas and bare land with fewer samples. Additionally, the proposed classification model significantly improved the discrimination of others from the rest of the land types for the dryland region. According to the accuracy assessment, identification of others is the most challenging classification task for all the comparison datasets; our findings indicated that training a specific model based on typical samples is effective to tackle that concern; this strategy can also be considered a potential solution to compensate for the large-scale mapping deficiencies in dryland regions.

The high-resolution remote sensing imagery adopted by this study provides abundant shape, texture, and spatial distribution information of landscapes, which strongly supports land cover feature extraction via the deep structure of the InceptionV3 model. Rich feature extraction suggests a better performance of classification. To obtain as many object features as possible for a certain pixel, the InceptionV3 output captured wide texture and shape information from its 3×3 neighboring pixels, which can promote sparse distributed land separation from its surrounding land types. For instance, sparse built-up areas were easily misclassified as their surrounding land types in GlobeLand30, FROM-GLC 2017v1, and GLC_FCS30-2020; a small fraction of vegetation or cultivated land among the urbanized regions was also difficult to accurately identify for most of the comparison products. These misclassifications were significantly improved in InceptionV3-classified data.

The proposed model was also competent in identifying land types that might change during various seasons. In dryland regions, cultivated land and vegetation were often confused during the growing season because of their similar features; crop- or vegetation-covered regions may be misclassified as others during the nongrowing season. A minor misclassification occurred with the InceptionV3 model because Google Earth high-resolution imagery is a composite of yearly data merged from different dates throughout the year; land types at the same location may vary across different seasons. Compared with the selected products, the InceptionV3 model separated cultivated land and vegetation better based on deep texture information. Moreover, confusion among others and cultivated land and vegetation also significantly decreased through deep texture and shape feature analysis of the InceptionV3 model. Spectral reflectance similarity is a common phenomenon for different land types: it enhanced the difficulty of land cover classification using traditional spectral classification models. InceptionV3 adopted deep and rich features of land cover to conduct classification tasks, which is beneficial for alleviating spectral confusion to some extent.

4.3. Consistency Comparison with Current Study

Previous research pointed that the classification accuracy of current finer-resolution global cover products varied in different regions [63]; it was in line with our assessment because accuracies of all the comparison datasets were lower in dryland regions. The application of DL models is effective to improve land cover classification accuracy of dryland heterogenous areas. Similar research found the classification accuracy of bare land in the DL model was much higher (96.3%) than that in the random forest model (63.5%) [64]; our proposed model also consistently demonstrated significant accuracy improvements of the identification of others when compared to several global land cover datasets produced using shallow machine learning classification techniques. Another study achieved satisfactory results by employing a 2D CNN model trained on dryland samples to classify land cover for Lahore (OA = 94.8%) and Faisalabad (OA = 91.4%) city, which was very similar to our data (OA = 92.63%).

Overall, the performance of our model was close to several current related research studies, indicating the proposed workflow was reliable for dryland urban land cover classification.

4.4. Limitations and Future Work of This Study

Significant improvement has been achieved using a specific trained InceptionV3 model to classify dryland urban land cover. However, some limitations in this study still need to be further discussed. First, the classification process is fairly time-consuming. Taking Urumqi as an example, the study area of this city was approximately 1396 km^2: more than three billion pictures were obtained after image segmentation. Classification of these images cost nearly 81 h in the InceptionV3 model, indicating that for our proposed strategy, it is hard to meet the requirement of large-scale land cover mapping. Fortunately, one of the latest studies has developed a generalizable deep learning-based model with an unsupervised domain adaptation strategy. This model is expected to support large-scale land cover mapping [65], suggesting that an improved CNN model has the potential to handle tremendous land cover classification work. Second, the identification of water bodies is not very satisfactory. Considering that most water bodies are permanent, extracting their distribution from a reliable database before classification might improve the above concern.

5. Conclusions

This study applied specific dryland landscape samples to train an InceptionV3 classification model, aiming to provide a complementary solution for enhancing the accuracy of large-scale land cover mapping in dryland regions. The assessment showed that our proposed model is highly effective for land cover mapping in dryland cities based on its remarkable accuracy. In contrast to the emerging land cover products derived from spectral classification techniques combined with auxiliary information analysis or deep learning segmentation classification models, our method performed better in tackling the challenge of identifying spectral confusion land types accurately. Moreover, it can also promote sparse distributed land separation from its surrounding dominant land types. Nevertheless, the accuracy of water body identification is not as satisfactory as that of other land types, which needs to be improved in future research. The proposed workflow can only serve as a complementary strategy for global land cover mapping accuracy improvement; its application in large-scale land cover classification is constrained because of substantial computing resource requirements. Overall, the proposed classification workflow in this study can compensate for the insufficient accuracy of global land cover products in dryland regions. It also can provide reliable information to support urban land dynamics monitoring and sustainable urbanization management of dryland cities.

Author Contributions: W.L. and G.L. processed the data and prepared the manuscript. B.Z., J.G., H.L. and S.H. contributed to the discussion and revision of results. X.L. inspired our main ideas and wrote the manuscript. All the authors contributed to the writing and revision of the paper. All authors have read and agreed to the published version of the manuscript.

Funding: This work is supported by the National Natural Science Foundation of China (Grant No. 42201328), the Key Scientific Research Project of Henan Higher Education Institutions (Grant No. 23A170016), and the Major Science and Technology Program of Henan Province (Grant No. 232102210043).

Data Availability Statement: The data that support the findings of this study are available from the corresponding author upon reasonable request.

Conflicts of Interest: The authors declare no conflict of interest.

References

1. Huang, J.; Yu, H.; Guan, X.; Wang, G.; Guo, R. Accelerated dryland expansion under climate change. *Nat. Clim. Chang.* **2016**, *6*, 166–171. [CrossRef]
2. Sietz, D.; Lüdeke, M.K.; Walther, C. Categorisation of typical vulnerability patterns in global drylands. *Glob. Environ. Chang.* **2011**, *21*, 431–440. [CrossRef]
3. Yan, Y.; Zhang, C.; Hu, Y.; Kuang, W. Urban land-cover change and its impact on the ecosystem carbon storage in a dryland city. *Remote Sens.* **2016**, *8*, 6. [CrossRef]
4. Ren, Q.; He, C.; Huang, Q.; Shi, P.; Zhang, D.; Güneralp, B. Impacts of urban expansion on natural habitats in global drylands. *Nat. Sustain.* **2022**, *5*, 869–878. [CrossRef]
5. Hoover, D.L.; Bestelmeyer, B.; Grimm, N.B.; Huxman, T.E.; Reed, S.C.; Sala, O.; Seastedt, T.R.; Wilmer, H.; Ferrenberg, S. Traversing the wasteland: A framework for assessing ecological threats to drylands. *BioScience* **2020**, *70*, 35–47. [CrossRef]
6. Forget, Y.; Linard, C.; Gilbert, M. Supervised classification of built-up areas in sub-saharan african cities using landsat imagery and openstreetmap. *Remote Sens.* **2018**, *10*, 1145. [CrossRef]
7. Klein, I.; Gessner, U.; Kuenzer, C. Regional land cover mapping and change detection in Central Asia using MODIS time-series. *Appl. Geogr.* **2012**, *35*, 219–234. [CrossRef]
8. Pan, T.; Lu, D.; Zhang, C.; Chen, X.; Shao, H.; Kuang, W.; Chi, W.; Liu, Z.; Du, G.; Cao, L. Urban land-cover dynamics in arid China based on high-resolution urban land mapping products. *Remote Sens.* **2017**, *9*, 730. [CrossRef]
9. Middleton, N.J.; Sternberg, T. Climate hazards in drylands: A review. *Earth-Sci. Rev.* **2013**, *126*, 48–57. [CrossRef]
10. Liu, J.; Zhang, Z.; Xu, X.; Kuang, W.; Zhou, W.; Zhang, S.; Li, R.; Yan, C.; Yu, D.; Wu, S.; et al. Spatial patterns and driving forces of land use change in China during the early 21st century. *J. Geogr. Sci.* **2010**, *20*, 483–494. [CrossRef]
11. Song, X.; Hansen, M.C.; Stehman, S.V.; Potapov, P.V.; Tyukavina, A.; Vermote, E.F.; Townshend, J.R. Global land change from 1982 to 2016. *Nature* **2018**, *560*, 639–643. [CrossRef]
12. Chen, J.; Cao, X.; Peng, S.; Ren, H. Analysis and applications of GlobeLand30: A review. *ISPRS Int. J. Geo-Inf.* **2017**, *6*, 230. [CrossRef]
13. Sun, B.; Chen, X.; Zhou, Q. Uncertainty Assessment of GlobeLand30 land cover dataset over Central Asia. *ISPRS-Int. Arch. Photogramm. Remote Sens. Spat. Inf. Sci.* **2016**, *41*, 1313–1317. [CrossRef]
14. Bie, Q.; Shi, Y.; Li, X.; Wang, Y. Contrastive Analysis and Accuracy Assessment of Three Global 30 m Land Cover Maps Circa 2020 in Arid Land. *Sustainability* **2023**, *15*, 741. [CrossRef]
15. See, L.; Laso Bayas, J.; Schepaschenko, D.; Perger, C.; Dresel, C.; Maus, V.; Salk, C.; Weichselbaum, J.; Lesiv, M.; McCallum, I. LACO-Wiki: A new online land cover validation tool demonstrated using GlobeLand30 for Kenya. *Remote Sens.* **2017**, *9*, 754. [CrossRef]
16. Yu, L.; Wang, J.; Li, X.; Li, C.; Zhao, Y.; Gong, P. A multi-resolution global land cover dataset through multisource data aggregation. *Sci. China Earth Sci.* **2014**, *57*, 2317–2330. [CrossRef]
17. Song, X.; Sexton, J.O.; Huang, C.; Channan, S.; Townshend, J.R. Characterizing the magnitude, timing and duration of urban growth from time series of Landsat-based estimates of impervious cover. *Remote Sens. Environ.* **2016**, *175*, 1–13. [CrossRef]
18. Li, W.; Dong, R.; Fu, H.; Wang, J.; Yu, L.; Gong, P. Integrating Google Earth imagery with Landsat data to improve 30-m resolution land cover mapping. *Remote Sens. Environ.* **2020**, *237*, 111563. [CrossRef]
19. Liu, X.; Hu, G.; Chen, Y.; Li, X.; Xu, X.; Li, S.; Pei, F.; Wang, S. High-resolution multi-temporal mapping of global urban land using Landsat images based on the Google Earth Engine Platform. *Remote Sens. Environ.* **2018**, *209*, 227–239. [CrossRef]
20. Guo, H.; Liu, Z.; Jiang, H.; Wang, C.; Liu, J.; Liang, D. Big Earth Data: A new challenge and opportunity for Digital Earth's development. *Int. J. Digit. Earth* **2017**, *10*, 1–12. [CrossRef]
21. Li, X.; Zheng, D.; Feng, M.; Chen, F. Information geography: The information revolution reshapes geography. *Sci. China Earth Sci.* **2022**, *65*, 379–382. [CrossRef]
22. Feng, M.; Li, X. Land cover mapping toward finer scales. *Sci. Bull.* **2020**, *65*, 1604–1606. [CrossRef]
23. Yang, C.; Huang, Q.; Li, Z.; Liu, K.; Hu, F. Big Data and cloud computing: Innovation opportunities and challenges. *Int. J. Digit. Earth* **2017**, *10*, 13–53. [CrossRef]

24. Kussul, N.; Lavreniuk, M.; Skakun, S.; Shelestov, A. Deep Learning Classification of Land Cover and Crop Types Using Remote Sensing Data. *IEEE Geosci. Remote Sens. Lett.* **2017**, *14*, 778–782. [CrossRef]
25. Li, X.; Feng, M.; Ran, Y.; Su, Y.; Liu, F.; Huang, C.; Shen, H.; Xiao, Q.; Su, J.; Yuan, S.; et al. Big Data in Earth system science and progress towards a digital twin. *Nat. Rev. Earth Environ.* **2023**, *4*, 319–332. [CrossRef]
26. Mahdianpari, M.; Salehi, B.; Rezaee, M.; Mohammadimanesh, F.; Zhang, Y. Very deep convolutional neural networks for complex land cover mapping using multispectral remote sensing imagery. *Remote Sens.* **2018**, *10*, 1119. [CrossRef]
27. Shelestov, A.; Lavreniuk, M.; Kussul, N.; Novikov, A.; Skakun, S. Exploring Google Earth Engine Platform for Big Data Processing: Classification of Multi-Temporal Satellite Imagery for Crop Mapping. *Front. Earth Sci.* **2017**, *5*, 17. [CrossRef]
28. Huang, B.; Zhao, B.; Song, Y. Urban land-use mapping using a deep convolutional neural network with high spatial resolution multispectral remote sensing imagery. *Remote Sens. Environ.* **2018**, *214*, 73–86. [CrossRef]
29. Zhu, Q.; Guo, X.; Deng, W.; Shi, S.; Guan, Q.; Zhong, Y.; Zhang, L.; Li, D. Land-use/land-cover change detection based on a Siamese global learning framework for high spatial resolution remote sensing imagery. *ISPRS J. Photogramm. Remote Sens.* **2022**, *184*, 63–78. [CrossRef]
30. Memon, N.; Parikh, H.; Patel, S.B.; Patel, D.; Patel, V.D. Automatic land cover classification of multi-resolution dualpol data using convolutional neural network (CNN). *Remote Sens. Appl. Soc. Environ.* **2021**, *22*, 100491. [CrossRef]
31. Wambugu, N.; Chen, Y.; Xiao, Z.; Wei, M.; Bello, S.A.; Junior, J.M.; Li, J. A hybrid deep convolutional neural network for accurate land cover classification. *Int. J. Appl. Earth Obs. Geoinf.* **2021**, *103*, 102515. [CrossRef]
32. Luo, M.; Ji, S. Cross-spatiotemporal land-cover classification from VHR remote sensing images with deep learning based domain adaptation. *ISPRS J. Photogramm. Remote Sens.* **2022**, *191*, 105–128. [CrossRef]
33. Zhang, C.; Sargent, I.; Pan, X.; Li, H.; Gardiner, A.; Hare, J.; Atkinson, P.M. Joint Deep Learning for land cover and land use classification. *Remote Sens. Environ.* **2019**, *221*, 173–187. [CrossRef]
34. Ali, K.; Johnson, B.A. Land-Use and Land-Cover Classification in Semi-Arid Areas from Medium-Resolution Remote-Sensing Imagery: A Deep Learning Approach. *Sensors* **2022**, *22*, 8750. [CrossRef] [PubMed]
35. LeCun, Y.; Bengio, Y.; Hinton, G. Deep learning. *Nature* **2015**, *521*, 436. [CrossRef] [PubMed]
36. Zhu, Z.; Zhang, Z.; Zuo, L.; Pan, T.; Zhao, X.; Wang, X.; Sun, F.; Xu, J.; Liu, Z. Study on the Classification and Change Detection Methods of Drylands in Arid and Semi-Arid Regions. *Remote Sens.* **2022**, *14*, 1256. [CrossRef]
37. Weng, L.; Qian, M.; Xia, M.; Xu, Y.; Li, C. Land use/land cover recognition in arid zone using A multi-dimensional multi-grained residual Forest. *Comput. Geosci.* **2020**, *144*, 104557. [CrossRef]
38. Ge, G.; Shi, Z.; Zhu, Y.; Yang, X.; Hao, Y. Land use/cover classification in an arid desert-oasis mosaic landscape of China using remote sensed imagery: Performance assessment of four machine learning algorithms. *Glob. Ecol. Conserv.* **2020**, *22*, e00971. [CrossRef]
39. Abida, K.; Barbouchi, M.; Boudabbous, K.; Toukabri, W.; Saad, K.; Bousnina, H.; Sahli Chahed, T. Sentinel-2 Data for Land Use Mapping: Comparing Different Supervised Classifications in Semi-Arid Areas. *Agriculture* **2022**, *9*, 1429. [CrossRef]
40. Huang, J.; Ji, M.; Xie, Y.; Wang, S.; Ran, J. Global semi-arid climate change over last 60 years. *Clim. Dyn.* **2016**, *46*, 1131–1150. [CrossRef]
41. He, C.; Liu, Z.; Gou, S.; Zhang, Q.; Zhang, J.; Xu, L. Detecting global urban expansion over the last three decades using a fully convolutional network. *Environ. Res. Lett.* **2019**, *14*, 034008. [CrossRef]
42. Hassan, G.Z.; Hassan, F.R.; Akhtar, S. Environmental Issues and Concerns of Groundwater in Lahore. *Proc. Pak. Acad. Sci. B. Life Environ. Sci.* **2016**, *53*, 163–178.
43. Liu, T.; Chen, X. Application of deep learning in GlobeLand30-2010 product refinement. *Int. Arch. Photogramm. Remote Sens. Spat. Inf. Sci.* **2018**, *42*, 1111–1116. [CrossRef]
44. Pashaei, M.; Kamangir, H.; Starek, M.J.; Tissot, P. Review and evaluation of deep learning architectures for efficient land cover mapping with UAS hyper-spatial imagery: A case study over a wetland. *Remote Sens.* **2020**, *12*, 959. [CrossRef]
45. Pires de Lima, R.; Marfurt, K. Convolutional neural network for remote-sensing scene classification: Transfer learning analysis. *Remote Sens.* **2019**, *12*, 86. [CrossRef]
46. Gao, L.; Luo, J.; Xia, L.; Wu, T.; Sun, Y.; Liu, H. Topographic constrained land cover classification in mountain areas using fully convolutional network. *Int. J. Remote Sens.* **2019**, *40*, 7127–7152. [CrossRef]
47. Chollet, F. Xception: Deep learning with depthwise separable convolutions. In Proceedings of the IEEE Conference on Computer Vision and Pattern Recognition, Honolulu, HI, USA, 21–26 July 2017; pp. 1251–1258.
48. Luan, W.; Li, X. Rapid urbanization and its driving mechanism in the Pan-Third Pole region. *Sci. Total Environ.* **2021**, *750*, 141270. [CrossRef]
49. Tong, X.; Xia, G.; Lu, Q.; Shen, H.; Li, S.; You, S.; Zhang, L. Land-cover classification with high-resolution remote sensing images using transferable deep models. *Remote Sens. Environ.* **2020**, *237*, 111322. [CrossRef]
50. Castelluccio, M.; Poggi, G.; Sansone, C.; Verdoliva, L. Land use classification in remote sensing images by convolutional neural networks. *arXiv* **2015**, arXiv:1508.00092.
51. Cheng, C.; Yang, X.; Cai, H. Analysis of Spatial and Temporal Changes and Expansion Patterns in Mainland Chinese Urban Land between 1995 and 2015. *Remote Sens.* **2021**, *13*, 2090. [CrossRef]
52. Yang, H.; Li, S.; Chen, J.; Zhang, X.; Xu, S. The standardization and harmonization of land cover classification systems towards harmonized datasets: A review. *ISPRS Int. J. Geo-Inf.* **2017**, *6*, 154. [CrossRef]

53. Fritz, S.; See, L.; Perger, C.; McCallum, I.; Schill, C.; Schepaschenko, D.; Duerauer, M.; Karner, M.; Dresel, C.; Laso-Bayas, J.-C. A global dataset of crowdsourced land cover and land use reference data. *Sci. Data* **2017**, *4*, 170075. [CrossRef] [PubMed]
54. Tilahun, A.; Teferie, B. Accuracy assessment of land use land cover classification using Google Earth. *Am. J. Environ. Prot.* **2015**, *4*, 193–198. [CrossRef]
55. Chen, J.; Chen, J.; Liao, A.; Cao, X.; Chen, L.; Chen, X.; He, C.; Han, G.; Peng, S.; Lu, M. Global land cover mapping at 30 m resolution: A POK-based operational approach. *ISPRS J. Photogramm. Remote Sens.* **2015**, *103*, 7–27. [CrossRef]
56. Gong, P.; Wang, J.; Yu, L.; Zhao, Y.; Zhao, Y.; Liang, L.; Niu, Z.; Huang, X.; Fu, H.; Liu, S. Finer resolution observation and monitoring of global land cover: First mapping results with Landsat TM and ETM+ data. *Int. J. Remote Sens.* **2013**, *34*, 2607–2654. [CrossRef]
57. Zhang, X.; Liu, L.; Chen, X.; Gao, Y.; Xie, S.; Mi, J. GLC_FCS30: Global land-cover product with fine classification system at 30 m using time-series Landsat imagery. *Earth Syst. Sci. Data* **2021**, *13*, 2753–2776. [CrossRef]
58. Karra, K.; Kontgis, C.; Statman-Weil, Z.; Mazzariello, J.C.; Mathis, M.; Brumby, S.P. Global land use/land cover with Sentinel 2 and deep learning. In Proceedings of the 2021 IEEE International Geoscience and Remote Sensing Symposium IGARSS, Brussels, Belgium, 11–16 July 2021; pp. 4704–4707.
59. Van De Kerchove, R.; Zanaga, D.; Keersmaecker, W.; Souverijns, N.; Wevers, J.; Brockmann, C.; Grosu, A.; Paccini, A.; Cartus, O.; Santoro, M. ESA WorldCover: Global Land Cover Mapping at 10 m Resolution for 2020 Based on Sentinel-1 and 2 Data. In Proceedings of the AGU Fall Meeting Abstracts, 2021; p. GC45I-0915. Available online: https://ui.adsabs.harvard.edu/abs/2021AGUFMGC45I0915V/abstract (accessed on 13 December 2021).
60. Tsendbazar, N.E.; de Bruin, S.; Herold, M. Integrating global land cover datasets for deriving user-specific maps. *Int. J. Digit. Earth* **2017**, *10*, 219–237. [CrossRef]
61. Foody, G.M. Explaining the unsuitability of the kappa coefficient in the assessment and comparison of the accuracy of thematic maps obtained by image classification. *Remote Sens. Environ.* **2020**, *239*, 111630. [CrossRef]
62. Landis, J.R.; Koch, G.G. The measurement of observer agreement for categorical data. *Biometrics* **1977**, *33*, 159–174. [CrossRef]
63. Liu, L.; Zhang, X.; Gao, Y.; Chen, X.; Shuai, X.; Mi, J. Finer-resolution mapping of global land cover: Recent developments, consistency analysis, and prospects. *J. Remote Sens.* **2021**, *2021*, 5289697. [CrossRef]
64. Mountrakis, G.; Heydari, S.S. Harvesting the Landsat archive for land cover land use classification using deep neural networks: Comparison with traditional classifiers and multi-sensor benefits. *ISPRS J. Photogramm. Remote Sens.* **2023**, *200*, 106–119. [CrossRef]
65. Tong, X.Y.; Xia, G.S.; Zhu, X.X. Enabling country-scale land cover mapping with meter-resolution satellite imagery. *ISPRS J. Photogramm. Remote Sens.* **2023**, *196*, 178–196. [CrossRef] [PubMed]